## Supplementary Information

# Experimental and Computational Investigation into the Hydrodynamics and Chemical Dynamics of Laser Ablation Aluminum Plasmas

Emily H. Kwapis[1], Jacob W. Posey[2], Enrique Medici[1], Kira Berg[3], Ryan W. Houim[2], and Kyle C. Hartig[1]

[1]Nuclear Engineering Program, Department of Materials Science and Engineering, University of Florida, Gainesville, FL 32611
[2]Department of Mechanical and Aerospace Engineering, University of Florida, Gainesville, FL 32611
[3]Department of Agricultural and Biological Engineering, University of Florida, Gainesville, FL 32611

Corresponding Author E-mail: ekwapis@ufl.edu

## Characterization of the Ablation Crater and Corresponding Effect on Fireball Expansion Dynamics

Measurement of the ablation crater was performed using a Brucker optical profilometer to determine crater dimensions to input into the HyBurn simulation. Material is shown to fill the central portion of the crater (see Fig. 1), and the impact of this central island feature on the properties and expansion dynamics of the fireball in computational simulations was investigated in comparison to a simplified crater design (see Fig. 2). There was no observable change in fireball properties (e.g., temperature, pressure, mass fractions) between the two craters and the spatio-temporal evolution of the fireballs remained comparable. Runtimes were doubled for the central island crater, therefore, HyBurn simulations discussed in the journal article use the basic crater design.

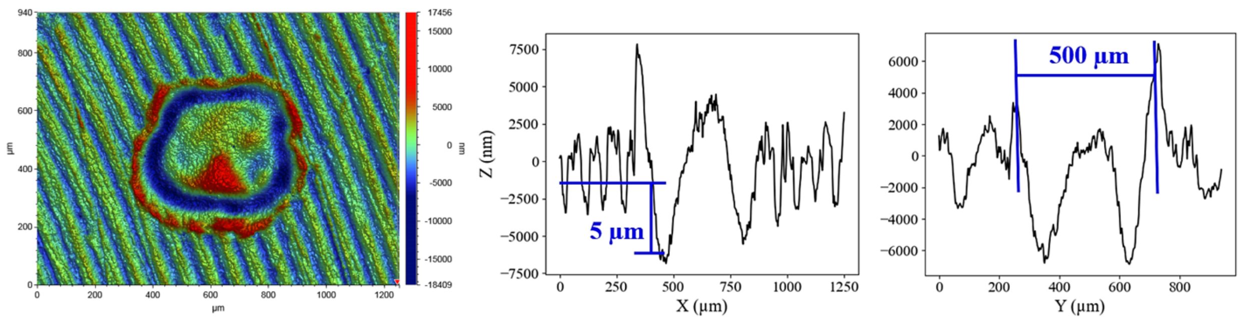


Figure 1. 2D image and cross-sections through the mid-plane of the laser ablation crater measured using an optical profilometer. Oscillations on the surface height on either side of the crater represent machining marks on the sample.

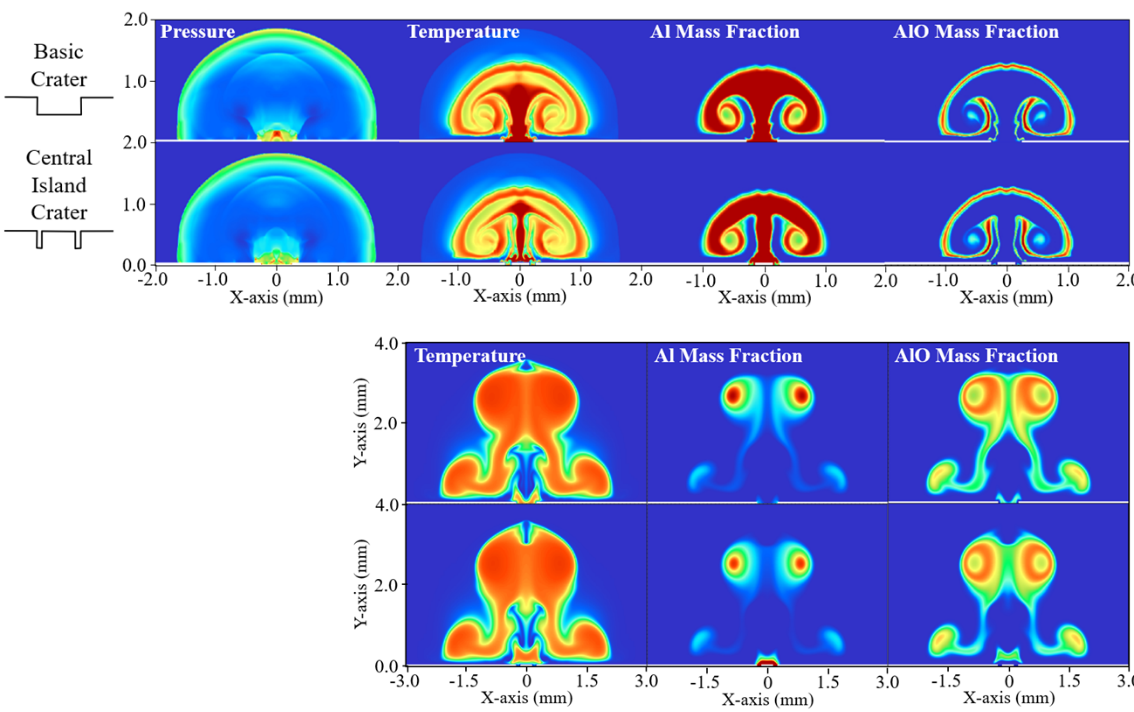


Figure 2. Comparison between HyBurn fireball properties for different ablation crater morphologies. The top set of images corresponds to a simulation time of 1 µs while the bottom set corresponds to 20 µs. Colormaps are scaled by column at their respective simulation times.

## Plasma Temperature Estimation using PGopher

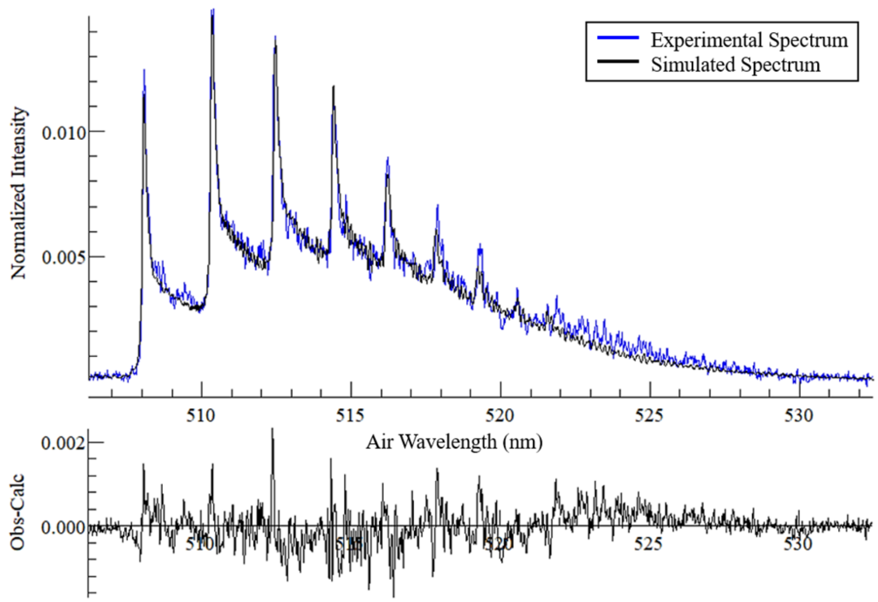


Figure 3. Example of contour fitting results in PGopher using the $\Delta v = -1$ band of the AlO $B^2\Sigma^+$-$X^2\Sigma^+$ transition at an experimental time delay of 50 µs. Based on the theoretical fit, the plasma temperature was estimated to be 3594.45 $\pm$ 28.42 K.

## Fitting Shockwave Expansion Models to Shadowgraphic Data

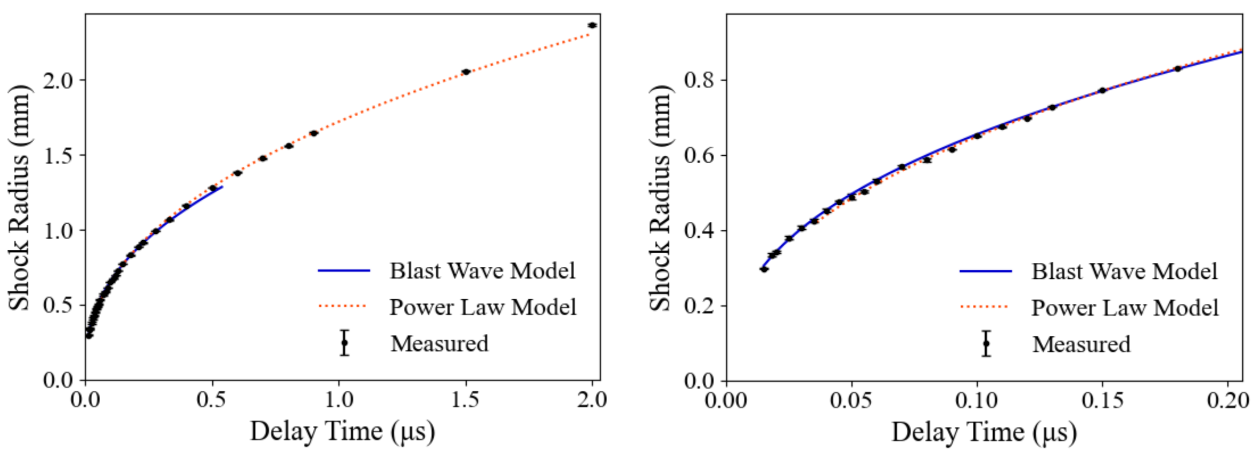


Figure 4. Expansion model fits to the measured shock front trajectory. The optimization domain for the Sedov-Taylor blast wave model covers the first 40 ns and the shock radius was found to follow the relationship (magnified figure on the right). The expansion model fit determined for later delay times follows a power law relationship and is given by .

**Data on Reaction Mechanisms and Kinetics**

Forward reaction rate constants $k^{+}$ given in Table 1 follow the Arrhenius formula,

$$k^{+} = AT^{n}\exp\left(-\frac{E_a}{T}\right) \#(S1)$$

where $A$ is the pre-exponential factor, $n$ is the power coefficient, $E_a$ is the activation energy, and $T$ is the temperature.

Table 1. Reaction mechanisms and rate coefficients used in the computational model. Species exist in the gas-phase unless noted otherwise. (Units: cm, mol, s, K)

| | | Rate Constants | | | |
|---|---|---|---|---|---|
| No. | Reaction | A | n | $E_a$ | Ref. |
| 1 | $Al + O_2 \leftrightarrow AlO + O$ | $2.31 \cdot 10^{13}$ | | 0 | [1] |
| 2 | $Al + O + M \leftrightarrow AlO + M$ | $3 \cdot 10^{17}$ | | 0 | [2] |
| 3 | $AlO + O_2 \leftrightarrow AlO_2 + O$ | $7.12 \cdot 10^{12}$ | | 13,150 | [1] |
| 4 | $AlO_2 \leftrightarrow AlO + O$ | $1 \cdot 10^{15}$ | | 44,564.6 | [1] |
| 5 | $Al_2O \leftrightarrow AlO + Al$ | $1 \cdot 10^{15}$ | | 67,035.7 | [1] |
| 6 | $Al_2O_2 \leftrightarrow AlO + AlO$ | $1 \cdot 10^{15}$ | | 59,335.7 | [1] |
| 7 | $Al_2O_2 \leftrightarrow Al + AlO_2$ | $1 \cdot 10^{15}$ | | 74,937.1 | [1] |
| 8 | $Al_2O_2 \leftrightarrow Al_2O + O$ | $1 \cdot 10^{15}$ | | 52,466 | [1] |
| 9 | $Al_2O_3 \leftrightarrow Al_2O_2 + O$ | $3 \cdot 10^{15}$ | | 49,144.4 | [1] |
| 10 | $Al_2O_3 \leftrightarrow AlO_2 + AlO$ | $3 \cdot 10^{15}$ | | 63,915.4 | [1] |
| 11 | $Al_2O_3 \leftrightarrow Al_2O_3$ (l) | $1 \cdot 10^{14}$ | | 0 | [1] |
| 12 | $O_2 + M \leftrightarrow O + O + M$ | $2 \cdot 10^{21}$ | | 59,360 | [3] |
| 13 | $O_2 + N \leftrightarrow NO + O$ | $2.49 \cdot 10^{9}$ | | 4,010 | [3] |
| 14 | $N_2 + M \leftrightarrow N + N + M$ | $7 \cdot 10^{21}$ | | 113,200 | [3] |
| 15 | $N_2 + O \leftrightarrow NO + N$ | $6 \cdot 10^{13}$ | | 38,000 | [3] |
| 16 | $NO + M \leftrightarrow N + O + M$ | $2 \cdot 10^{15}$ | | 75,500 | [3] |

References: [1] A.M. Starik *et al.*, *Combust. Flame* **161**, 1659-1667 (2014). [2] B.T. Bojko *et al.*, *Combust. Flame* **161**, 3211-3221 (2014). [3] C.O. Johnston and A.M. Brandis, *JQSRT* **149**, 303-317 (2014).